IMPURITIES IN SOLAR-GRADE SILICON AND THEIR CHARACTERISATION

Daniel Macdonald[1], Jason Tan[1], Robert Bardos[2] and Thorsten Trupke[2]
[1]Department of Engineering, College of Engineering and Computer Science, The Australian National University, Canberra ACT 0200, Australia. Tel: +61 (0)2 6125 2973, Fax: +61 (0)2 6125 0506, email: Daniel.Macdonald@anu.edu.au.
[2]Centre of Excellence for Advanced Silicon Photovoltaics and Photonics, University of New South Wales, Sydney, 2052, NSW, Australia. Tel.: +61 (0)2 9385 4054, Fax: +61 (0)2 9662 4240, email: thorsten@trupke.de.

ABSTRACT: Impurities can play a significant role in reducing the efficiency of crystalline silicon solar cells. Here we review the most important impurities in directionally-solidified ingot-grown multicrystalline silicon, and the most commonly used techniques to detect them. We also introduce a new method for creating images of the interstitial iron concentration in silicon wafers using photoluminescence imaging. This technique has the potential to generate fast, high resolution iron images under injection conditions that avoid unwanted dissociation of iron-boron pairs.
Keywords: Silicon, Metal Impurities, Photoluminescence

1 INTRODUCTION

Unintentional impurities have a significant negative impact in today's solar-grade silicon materials such as multicrystalline silicon. With the advent of low-cost solar-grade silicon feedstocks, this is likely to remain the case well into the medium term. The purpose of this paper is to review the most important of these impurities and the methods that have been successfully used to detect them. In addition, we demonstrate a method for rapid imaging of interstitial iron concentrations in silicon wafers, one of the most important metallic impurities. The technique is based on taking high resolution photoluminescence images before and after dissociating FeB pairs.

2 IMPURITIES IN SOLAR-GRADE SILICON

Not surprisingly, the type and concentration of impurities present in silicon materials for photovoltaics depends very strongly on the growth technique. At one extreme, today's very pure single-crystal silicon wafers grown by the float-zone method are effectively impurity-free in terms of recombination. Generally, solar cells made with such material are limited by recombination at the surfaces and diffused regions, or by Auger recombination in the base, unless bulk contamination occurs during cell fabrication. Next in line, most Czochralski silicon is also effectively metal-free in terms of recombination, but is prone to the well-known B-O defect [1]. This occurs due to the relatively high levels of dissolved oxygen derived from the quartz crucibles that contain the silicon melt.

Multicrystalline silicon materials made especially for photovoltaics include ingot-grown materials (most commonly directionally-solidified), and sheet and ribbon silicon (grown vertically without a substrate, for example edge-defined Film-fed Growth (EFG) and String Ribbon, or grown horizontally on a substrate, for example Ribbon-Grown Silicon (RGS) and SiliconFilm), as discussed in detail in Ref. [2]. These tend to contain a significant number of impurities that derive from the foreign materials (crucible walls and linings, supporting substrates) in direct contact with the molten silicon. Finally, polysilicon thin films formed by crystallising amorphous films deposited on foreign substrates, such as CSG silicon, also contain significant quantities of impurities [3].

In this paper we will focus on directionally-solidified ingot-grown multicrystalline silicon, the most common material for photovoltaics. More detailed information on impurities in other solar-grade forms of silicon can be found in Refs. [2,3,4], although in many cases the impurities and techniques used to detect them are the same as those presented here.

The fundamental mechanisms which determine the distribution of impurities in an ingot are segregation and diffusion. Most impurities have segregation coefficients less than unity, meaning they are more soluble in the liquid phase than the solid phase. This leads to higher concentrations in the top of a multicrystalline ingot (where crystallisation proceeds from the bottom). An exception is oxygen, which has the reverse trend. Shallow dopants tend to have segregation coefficients not much less than unity, leading to relatively gentle increases towards the top of an ingot. Most transition metals, however, have very small segregation coefficients. This in principle allows very effective segregation to the top of an ingot. In practice this is often reduced somewhat by the tendency of structural defects to enhance the incorporation of impurities into the solid phase than would occur otherwise [5,6].

A feature of ingot-grown multicrystalline silicon is the very long ingot cooling time, tens of hours typically. This allows for a re-distribution of impurities via solid-state diffusion from the original distribution generated by segregation. This is a significant factor in the commonly observed low lifetime regions seen at the bottom and sides of such ingots, although disrupted crystal structure also contributes. Figure 1 shows profiles for some typical impurities in a multicrystalline silicon ingot, taken from Ref. [6], as measured by neutron activation analysis. The segregation towards the top of the ingot is clear in all cases, including boron, which has an effective segregation coefficient k_{eff} not far from unity (0.65), and is a slow diffuser. Solid-state diffusion from the bottom is also evident for the fast-diffusing metals Fe, Cu and Co.

Such data provides strong clues on the source of the metallic impurities in question. It is clear that the metals at the bottom of the ingot have come from the crucible walls and linings. It is also likely that most of the metals found at the top of the ingot have come from the same source. This seems feasible when considering that the silicon charge remains entirely molten for a considerable time before crystallisation begins, allowing impurities from the crucible to dissolve into the melt, which are subsequently segregated to the top during solidification.

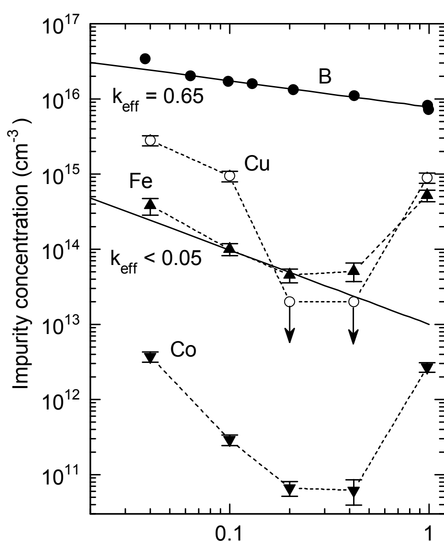

Figure 1: *Concentrations of B, Fe, Co, and Cu as a function of ingot position (fraction from top, hence 0 is the top, 1 the bottom). The straight lines are segregation model fits with k_{eff}=0.65 for B and k_{eff}<0.05 for Fe. From Ref. [6].*

Note that the peak concentrations at the bottom and top are similar, as is the amount of time available for both dissolution into the melt and solid-state in-diffusion. Note also that the order of concentration of the three metal impurities is similar at the top and bottom (i.e Cu, then Fe, then Co), again indicating that they come from the same source: the crucible (perhaps from previous crucibles if ingot tops and bottoms are recycled).

In the following sections we examine three different categories of impurities in directionally-solidified ingot-grown multicrystalline silicon in more detail: metal impurities; oxygen, carbon and nitrogen; and the shallow dopants.

3 METAL IMPURITIES

Unwanted metallic impurities are the cause of a large fraction of the total recombination events in solar cells made from materials such as multicrystalline silicon. These metals may be present in a number of different chemical forms, such as point-like (interstitial or substitutional), or in precipitates, which often form at structural defects such as grain boundaries, dramatically increasing their recombination activity.

In directionally-solidified ingot-grown multicrystalline silicon, the most abundant appear to be Fe, Ni and Cu, and to a lesser degree Cr, Co and Mo [2,4,6,7,8,9]. Others such as Mn, Ti , Zn and V have also been detected in such materials, although generally at fairly low concentrations [2,4,9].

3.1 Chemical states and recombination activity

Most transition metals occur as interstitial impurities when present in silicon below the solid-solubility limit. Ni, Cu and Co are such rapid diffusers that they almost always completely precipitate out at surfaces or internal defects during cooling after ingot growth or cell processing. Some small fraction of these impurities may remain frozen-in in substitutional form, but if they do, there is little evidence of their impact in photovoltaic silicon materials.

Impurities with moderate diffusivities, such as Fe, Cr, and Mn, tend to mostly precipitate as well, as shown, for example, by synchrotron-based methods [2,10]. They tend to co-precipitate at the same sites as Ni and Cu, forming alloyed silicides [2]. However, they usually retain a small but detectible fraction in interstitial form after typical high temperature steps, since at a certain temperature they can no longer reach a favourable precipitation site before being effectively frozen-in. For example, approximately 1% of Fe in as-grown mc-Si wafers exists in interstitial from, while the rest is precipitated, mostly at structural defects [6]. Nevertheless, this small interstitial fraction has a significant impact on the overall carrier lifetime.

Fe, Cr and Mn remain very slightly mobile even at room temperature, giving rise to their well-known property of forming pairs with positively-charged ionised dopant atoms such as B, Ga and Al [11]. The ability to easily toggle between the paired and un-paired states, which have different recombination properties, permits very sensitive detection of these interstitial impurities in silicon via carrier lifetime or diffusion length measurements [12]. Like many transition metals, Fe and Cr carry a positive charge when ionised in crystalline silicon. This helps drive the coulombic attraction to the negatively-charged dopant atoms. It also means that they are more attractive as traps to electrons, which in turn leads to greater recombination activity in *p*-type silicon (in which electrons are minority carriers) than in *n*-type silicon [13]. The moderate diffusivity of these impurities at typical processing temperatures means that they can be effectively gettered by phosphorus or aluminium diffusions.

Very slowly diffusing impurities such as Ti, Mo and V remain more evenly distributed during ingot growth, unless originally present as undissolved inclusions in the melt [2]. A larger fraction is likely to remain in interstitial form and un-precipitated than is the case for Fe, Cr and Mn. Nevertheless, they are also detected at precipitates [2], often in the company of the faster diffusing metals above. Despite having positive charge states in the interstitial form, they do not form pairs with dopant atoms because they are effectively completely immobile at room temperature. Their low diffusivity also means they are impervious to gettering at temperatures and times typically used for device processing.

Naturally, point-like metals in general have greater recombination strength ‘per atom’ than precipitated metal atoms, since the latter are co-located. This highlights the importance of the distribution and chemical state of impurities, rather than simply their total average concentration. It also offers the prospect of defect engineering, in which appropriate treatments could be developed to coax the impurities into their most benign distribution and chemical state.

3.2 Characterisation techniques

The challenge in detecting metal impurities in multicrystalline silicon wafers lies in their relatively low concentrations, typically in the range of 10^{10} to 10^{15}cm^{-3}. In some cases mass spectroscopy techniques such as Secondary Ion Mass Spectroscopy (SIMS), Glow-Discharge Mass Spectroscopy (GDMS) or Inductively-Coupled Plasma Mass Spectroscopy (ICP-MS), can be used effectively. Generally though, they are only

successful for the most heavily contaminated samples, or if the contaminants are concentrated, for example, in the near-surface region via phosphorus gettering. SIMS has been successfully used to reveal the effectiveness of such gettering in removing native impurities in mc-Si such as Fe, Cr, Cu and Ni [9,14], or, using highly focussed ion beams, for studying impurities segregated to grain boundaries [15]. Such techniques reveal the total concentration of metals, irrespective of their chemical state.

Techniques based on tightly focussed synchrotron radiation have also been successfully applied to metal impurities in mc-Si, and other solar-grade materials [2,7,8,10]. X-ray Fluorescence Spectroscopy (XFS) with a high resolution microprobe (beam size below 1 micron), has been used to detect metals in precipitates, courtesy of their locally high concentrations. Precipitates as small as several tens of nanometres have been detected in this way. This has revealed much about the size and distribution of such precipitates, and also their location in relation to structural defects such as grain boundaries. Applying X-ray Absorption Near-Edge Spectroscopy (XANES) with the same high spatial resolution can reveal the chemical state of such precipitates.

Another technique successfully applied to identifying metals in mc-Si is Neutron Activation Analysis [4,6]. This is more sensitive than the techniques above, but has little capacity for spatial resolution, and can not reveal information about chemical states. The sensitivity is also highly dependent on the target species, and can vary from around 10^{10} to 10^{14} cm^{-3}.

The most sensitive techniques for detecting metal impurities in semiconductors are based on electrical measurements. Deep-Level Transient Spectroscopy (DLTS) can in principle reach detection limits as low as $10^{-4}\times N_{A/D}$. However, it is generally used for detecting point-like impurities, and the presence of precipitates can make the interpretation of the spectra difficult [16,17]. Nevertheless, there have been a number of successful applications of DLTS to solar-grade multi- and poly-crystalline silicon wafers. These have identified, for example, oxygen-related levels and vanadium and chromium impurities in multicrystalline silicon [18,19], and interstitial Fe and Cr in EFG ribbon silicon [20,21] and in sheet silicon [22].

Finally, methods based on measuring the carrier lifetime before and after defect transformation can also be very sensitive for certain impurities in *p*-type silicon. The best known case is that of interstitial Fe, detected through diffusion length or lifetime measurements before and after FeB pair dissociation by strong illumination [12]. Detection limits as low as 10^{10} cm^{-3} can be reached in this way. The same approach has been used for interstitial Cr with thermal dissociation [19,23], and should also work for Mn. In a similar manner, the effective density of B-O centres in oxygen rich Si can be determined before and after defect activation via illumination [24].

4 OXYGEN, CARBON AND NITROGEN

These three impurities are ubiquitous in silicon materials, but fortunately are quite benign in terms of recombination. An important exception is the well-known B-O defect initially found in Cz silicon, but which also occurs to a lesser degree in mc-Si [24]. Oxygen also forms an active recombination centre with Al [25]. Excessive oxygen can lead to the formation of thermal donors and larger oxygen precipitates [18,26,27]. Interstitial oxygen concentrations are typically in the range of 5-10 ppma near the bottom of a mc-Si ingot, decreasing towards 1-3 ppma at the top [28]. In cases where it has exceeded 10 ppma, significant reductions in carrier lifetime and cell performance were observed [28]. Substitutional carbon concentrations are typically in the range 7-11 ppma [28]. If present in very high concentrations, carbon and nitrogen can form SiC and SiN inclusions within an ingot. These can cause wire breaking during wafering, or create conductive pathways than can potentially produce shunts across the *p-n* junction of a solar cell.

Fourier Transform InfraRed spectroscopy (FTIR) is used to directly detect interstitial O and substitutional C [29,30]. Interstitial nitrogen forms complexes with itself and oxygen which can also be detected by FTIR [31]. Due to their relatively high concentrations, total concentrations of these elements can be detected with mass spectroscopy methods such as SIMS, GDMS or ICP-MS, or also by Auger electron spectroscopy [15].

5 DOPANT IMPURITIES

Shallow dopants in silicon, such as B, Ga, Al, As and P, are mostly present in substitutional form. They are therefore very slow diffusers, but tend to have high solubility limits compared to interstitial metals. If present in super-saturated concentrations at high temperatures they may form agglomerates or small precipitates.

Shallow dopants form complexes with other impurities to generate important recombination centres, such as the Al-O and B-O defects mentioned above. They also form the stationary part of meta-stable metal-dopant pairs with Fe, Cr, Mn and Co [11]. Dopants are among the most difficult of the impurities to remove during feedstock production, due partly to their high solubility and segregation coefficients. This means that wafers made from new forms of solar-grade silicon feedstock are likely to be compensated to a greater extent than existing material. In principle, it is possible for shallow dopants to act as recombination centres in their own right. Generally this is not considered important since the recombination activity of majority carrier dopants is expected to be very slight, courtesy of their negligible interaction with the minority carrier band. However, compensated *minority* carrier dopant atoms may have significantly greater recombination strength based on their likely charge state [32]. Whether this is sufficient to have an impact in highly compensated material remains an open question.

Dopants are generally present in relatively high concentrations, hence their total concentrations are accessible by mass spectroscopy techniques such as SIMS, GDMS and ICP-MS. The fraction of electrically-active dopants can be inferred, for example, from conductance measurements for bulk concentrations, or from stripping Hall or C-V measurements for the near-surface region.

6 INTERSTITIAL IRON IMAGING WITH PHOTOLUMINESCENCE

As discussed above, interstitial iron (Fe_i) is an important impurity in solar-grade silicon materials such as ingot-grown multicrystalline silicon. The concentration of Fe_i can vary laterally across a wafer, and along the length of an ingot, and can also change dramatically during cell processing due to gettering, poisoning, precipitate formation and dissolution, and hydrogenation. It is therefore of considerable interest to be able to map changes in the iron concentration both laterally and during processing.

There are two main existing methods that can map the interstitial iron concentration in silicon wafers. The first, based on a method developed by Zoth and Bergholz [12], uses scanning Surface-PhotoVoltage (SPV) measurements of the change in low-injection carrier diffusion length upon dissociating iron-boron pairs in boron-doped *p*-type silicon [33,34,35]. Later, based on the same principle, Microwave-detected Photo-Conductance Decay (μW-PCD) maps of high-injection carrier lifetimes were used to generate iron maps, for example in Ref. [36]. Both these approaches use point-by-point mapping, and are hence quite slow. Also, SPV is not widely available in photovoltaic labs, and is often limited to cases where the diffusion length is shorter than the wafer thickness (which would not lead to a very efficient solar cell). The μW-PCD mapping technique is more widely available, but, in addition to being rather slow, is subject to some uncertainty regarding variations in injection-level, as discussed in detail below.

Therefore, a fast and robust method for imaging the interstitial iron concentration would be of considerable value. The use of lifetime imaging methods rather than point-by-point mapping methods would reduce the time required to obtain a high-resolution Fe-map from many hours to just minutes. This is in principle made possible by the recent advent of new methods for rapid imaging of carrier lifetimes in silicon wafers, namely Infrared-Lifetime Mapping (ILM) [37], also referred to as Carrier Density Imaging (CDI) [38], and Photoluminescence (PL) imaging [39]. In fact, Henze *et al.* [40] have recently used ILM to image interstitial iron concentrations in Ga-doped multicrystalline silicon wafers, revealing interesting effects near grain boundaries.

In this paper we introduce a method for such 'iron imaging' using photoluminescence images taken before and after dissociation of FeB pairs. An important consideration is the choice of injection-level used for the measurements. Low-injection offers the benefit of an injection-independent lifetime-to-iron concentration conversion factor *C*, a considerable simplification [41]. It also helps to ensure that minimal FeB pair splitting occurs during the measurements themselves. SPV operates in this regime, as could PL-based techniques, as they are immune to low-injection trapping-like artefacts that force other techniques such as μW-PCD and ILM to operate in mid- to high-injection [42]. On the other hand, high-injection provides better signal-to-noise ratios. However, the conversion factor used to transform the change in carrier lifetime upon dissociation of the FeB pairs into the local interstitial iron concentration [Fe_i], must then, in principle, be evaluated for each pixel, since it depends on the excess carrier density, which itself varies from pixel to pixel. In this work we have opted to perform our iron imaging under an illumination intensity of 1-sun, which gives rise to moderate injection levels. A method for calculating the local [Fe_i], pixel by pixel, has been developed, that accounts for changes in injection level before and after FeB pair dissociation.

We have firstly applied this iron imaging technique to a single-crystal float-zone wafer with distinct regions of varied but known concentrations of implanted iron. This has allowed us to verify that the technique generates reasonably accurate iron concentration images. We have then applied the method to as-cut multicrystalline silicon wafers containing various amounts of 'natural' iron, from different sections of a directionally-solidified ingot.

6.1 Experimental methods

A 'test' sample of 0.9 Ωcm boron-doped *p*-type float-zone silicon was prepared by ion implantation. After initial etching and cleaning, the sample was subjected to 3 overlapping implantations of 70keV Fe ions. Each implantation covered an area of 30 by 30 mm, and the doses used were 1×10^{11}, 3×10^{11} and 6×10^{11} cm^{-2}. The sample was lowered by 10 mm in between each implantation, resulting in 5 distinct regions with total Fe doses of 1×10^{11}, 4×10^{11}, 10×10^{11}, 9×10^{11} and 6×10^{11} cm^{-2}. The sample was then annealed at 1000 °C for 40 minutes in oxygen, growing a thin oxide that acts as a surface passivating layer. The wafer had a thickness of 0.025 cm, meaning that the implant doses correspond to Fe volume concentrations of 4×10^{12}, 1.6×10^{13}, 4×10^{13}, 3.6×10^{13} and 2.4×10^{13} cm^{-3}. The solubility of Fe at the anneal temperature is about 4×10^{14} cm^{-3} [43], which was intended to avoid precipitation of Fe during annealing. However, for safety reasons, the furnace was allowed to cool (rapidly) to 900 °C before unloading, at which temperature the solubility limit is closer to 4×10^{13} cm^{-3}. It is therefore possible that some precipitation may occur in the regions with the highest doses.

Boron-doped 1Ωcm (approximately) multicrystalline silicon (mc-Si) samples, 125 by 125 mm in size, were prepared by surface etching and cleaning, followed by plasma-enhanced chemical vapour-deposition of SiN films for surface passivation.

Photoluminescence images were taken with the system developed at UNSW, described in detail elsewhere [39]. Carrier generation was achieved with an 815 nm laser diode array. All images shown were collected for 1 second under '1 sun' illumination. FeB pair dissociation was achieved by illuminating the wafers with the laser diode array for 1 minute with 10 suns intensity. For the large mc-Si wafers this meant that only a smaller region within the wafer could be illuminated for pair dissociation.

6.2 Converting PL images into Fe images

Zoth and Bergholz [12] showed that the interstitial iron concentration [Fe_i] can be found via measurement of the carrier lifetime (or, equivalently, the diffusion length), before and after breaking FeB pairs in a boron-doped *p*-type silicon sample. The iron concentration is determined by [41]:

$$[Fe_i] = C\left(\frac{1}{\tau_1} - \frac{1}{\tau_0} \right)$$

where C is a constant, and τ_0 and τ_1 are the lifetimes measured before and after breaking the FeB pairs. A critical consideration is that the value of the conversion

factor C depends on the doping concentration and the injection level, or excess carrier density Δn, at which the two lifetime measurements are taken. Generally, it is best if the two lifetime measurements are taken at the same value of Δn. C also depends on the energy level and capture cross sections of the Fe_i and FeB states [41].

A powerful aspect of this technique is that the impact of other recombination channels, represented by τ_{other}, is subtracted out when the two recombination rates (inverse lifetimes) are subtracted. These other recombination channels may be due to surface defects or Auger recombination, for example. This means that iron measurements can be reliably taken on samples that contain other significant sources of recombination. However, this approach is only valid if these other channels are not altered by the FeB pair breaking process. It is also only strictly valid if the two lifetimes τ_0 and τ_1 are measured *at the same value of* Δn, since only then can we be sure that the value of τ_{other} is the same in both cases. This point is often overlooked.

An important point for any imaging or mapping technique, such as μW-PCD, ILM or PL imaging, is that they use only a single illumination intensity, or generation rate G. Since different regions of a sample have different lifetimes, the prevailing value of Δn will also vary across a sample. This means that, in principle, the C value needs to be determined for each pixel within a sample. Furthermore, the generation rate G is usually kept the same for the two lifetime measurements τ_0 and τ_1. Since the lifetime changes after FeB dissociation, the local value of Δn will also change upon dissociation.

In principle, these issues can be avoided when using lifetime methods such as ILM or PLI, since Δn is known, and therefore the appropriate values of C can be calculated pixel-by-pixel. There is a further problem however. Since Δn changes between τ_0 and τ_1, we can no longer be sure that τ_{other} is the same for both τ_0 and τ_1. This problem is *in principle* impossible to avoid for any method based on two lifetime measurements performed under the same generation rate, whether using μW-PCD, ILM or PL imaging. For practical reasons however, using a generation rate that is constant across a sample is the only feasible way to take such lifetime images. We can therefore only hope that such uncertainties remain small. This would certainly be true in cases where the lifetime is dominated by iron, and other recombination mechanisms and their injection-dependence thus play a minor role. It may not be true in very high-injection, where Auger recombination tends to dominate, and has a very strong injection-dependence. However, the impact of Auger recombination can also be subtracted out of the measurements, since its injection dependence is well known [44].

Fortunately, it is relatively straight-forward to calculate the appropriate 'effective' C value for each pixel when the two values of Δn before (Δn_0) and after (Δn_1) dissociation are known. One can show that the appropriate expression for the local interstitial iron concentration $[Fe_i]$ is then:

$$[Fe_i] = \frac{1}{\chi^{FeB} - \chi^{Fe_i}} \left[\frac{1}{\tau_0} - \frac{1}{\tau_1} - \frac{1}{\tau_{Auger0}} + \frac{1}{\tau_{Auger1}} \right]$$

where τ_{Auger0} and τ_{Auger1} are the Auger lifetimes at Δn_0 and Δn_1, calculated according to the general parameterisation in Ref. [44], and:

$$\chi^{FeB} = \frac{v_{th}(N_A + \Delta n_0)}{\frac{1}{\sigma_n^{FeB}}(N_A + \Delta n_0) + \frac{1}{\sigma_p^{FeB}}(n_1^{FeB} + \Delta n_0)},$$

$$\chi^{Fe_i} = \frac{v_{th}(N_A + \Delta n_1)}{\frac{1}{\sigma_n^{Fe_i}}(N_A + p_1^{Fe_i} + \Delta n_1) + \frac{\Delta n_1}{\sigma_p^{Fe_i}}},$$

where v_{th} is the thermal velocity, σ the capture cross sections (for electrons or holes, and for FeB or Fe_i), and p_1 and n_1 have their usual meanings in the Shockley-Read-Hall model. The capture cross sections and energy levels for FeB and Fe_i are taken from Ref. [45], except for σ_n^{Fei}, for which we have used a value of 1.3×10^{-14} cm^2. We have found that this value gives a better agreement with the implanted dose in the FZ sample. Note that since we are operating below the 'crossover point' in this case [41], our data is much more sensitive to this parameter than typical $[Fe_i]$ measurements performed at higher injection, for example with the QSSPC tool [41].

The only parameters that are to be determined from the PL images then are Δn_0 and Δn_1, and τ_0 and τ_1. The Δn values are determined by measuring the count rate on an optically-similar (or indeed the same) sample with known lifetime (measured by QSSPC) under a known generation rate. This allows the linear conversion factor between the PL count rate and Δn to be established. The τ values are then determined using $\Delta n = G\tau$.

Using the expressions above to calculate the local $[Fe_i]$ pixel by pixel accounts for the changing injection level and Auger recombination. These considerations are not generally taken account of in the application of μW-PCD to produce iron-maps. Indeed, it may be difficult to do so, since, being a differential lifetime technique, the true value of Δn is not always known. This would undoubtedly lead to some errors in Fe maps determined in this way, although the errors would hopefully be small.

6.3 Examples of iron imaging

Figure 2 shows PL images of the implanted FZ sample before and after FeB pair dissociation. The five regions of different Fe dose are evident, with the lightest dose on the right, and the heaviest in the middle. Note that the count rate has dropped dramatically after pair dissociation, indicating that the lifetime has also dropped. This reveals that the excess carrier density in this sample is below the so-called crossover point for FeB pairs (which is around $1\text{-}2\times10^{14}$ cm^{-3} for this resistivity). If the generation rate was increased enough to cause Δn to be *above* the crossover point, the PL intensity would increase after FeB pair dissociation. We did indeed observe this on the FZ sample. However, we found that it was difficult to avoid significant dissociation of FeB pairs during the first measurement when using illumination intensities significantly greater than 1 sun, which reduces the accuracy of the technique. Although the data collection time can be reduced in such cases, unfortunately the FeB dissociation rate increases approximately *quadratically* with intensity [46]. We therefore used 1 sun intensities in this work. Note that in

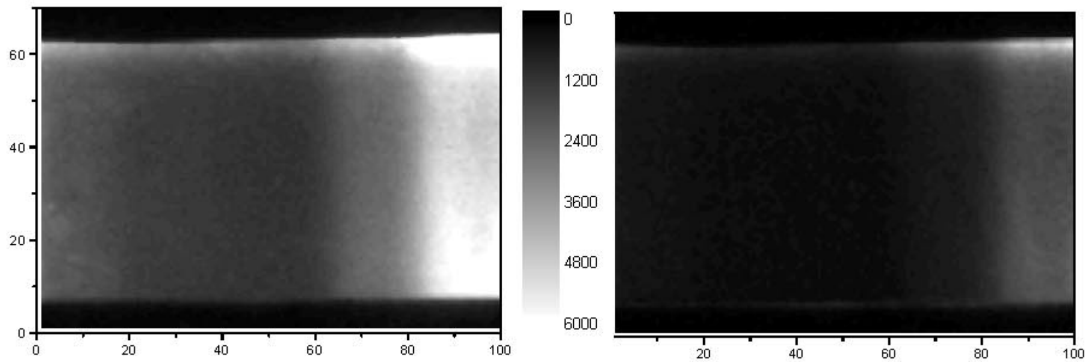

Figure 2: *PL images of the implanted FZ sample before (left) and after (right) FeB pair dissociation. The scale indicates the number of counts in the 1 second exposure time.*

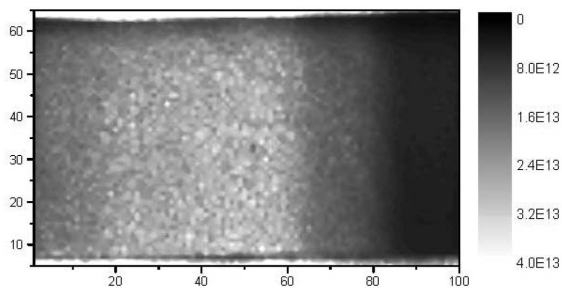

Figure 3: *Calculated iron image of the FZ sample, scale is in cm^{-3}.*

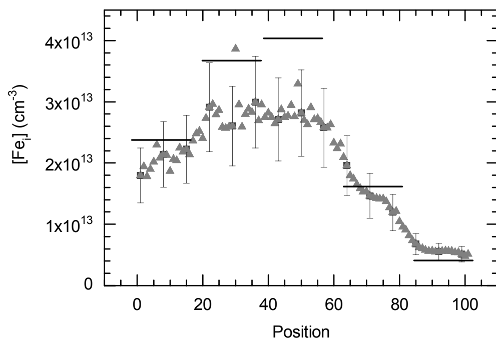

Figure 4: *Average Fe concentration from left to right for the FZ sample in Figure 3. The error bars represent the estimated uncertainty of 25%. The solid black lines represent the value of [Fe$_i$] expected from the ion dose.*

any case, one must take care that the prevailing injection level is not too close to the crossover point, as this dramatically reduces the sensitivity of the technique. For the FZ sample shown in Figure 2, the excess carrier densities were in the range 2×10^{12} to 5×10^{13} cm^{-3}, well below the crossover point.

Figure 3 shows the PL data converted into an iron image using the expression presented above. The [Fe$_i$] data is noisier that the raw PL count data, as may be expected from a quantity derived from the *difference* of two separate measurements. Figure 4 shows a profile of the measured [Fe$_i$] values derived by averaging line scans taken horizontally across Figure 3. The solid lines indicate the [Fe$_i$] values expected from the ion dose. This data is shown again in Figure 5, in the form of the average measured [Fe$_i$] for each region, versus that

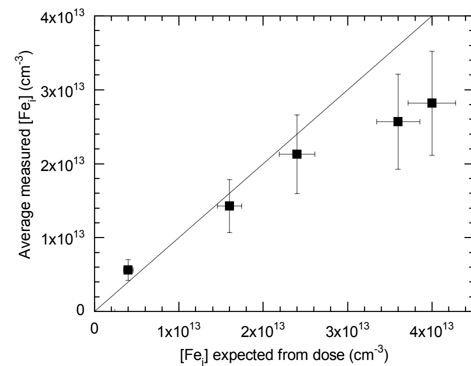

Figure 5: *Average measured [Fe$_i$] versus expected [Fe$_i$] from the ion dose.*

expected from the dose. The measurements are in reasonable agreement with the expected values for the three lower doses, within 25% as represented by the error bars. However, there is a systematic underestimation of the [Fe$_i$] for the two highest does, which could be due to precipitation of Fe$_i$ during cooling after annealing, as discussed above. In any case, these highest values are considerably higher than is generally encountered in multicrystalline wafers, so the technique should be applicable to this material.

Figure 6 shows the PL images of a mc-Si wafer before (left) and after (right) dissociation of FeB pairs. The dotted square on the right-hand image shows the region that was illuminated to break the FeB pairs. The lifetime, and hence count rate, in this region is clearly reduced. The small solid square represents the region analysed to generate an iron image.

Figure 7 shows this smaller region, firstly as the raw PL data (left), and also as an iron image (right). This wafer was from approximately 20% from the bottom of a mc-Si ingot, a region which usually contains significant quantities of interstitial iron. Note that the PL data on the left indicates that there are narrow regions near the grain boundaries that actually have *higher* lifetimes than deep within the grains, suggesting internal gettering of impurities to the grain boundaries during ingot cooling. This is mirrored in the iron image, which indeed indicates that interstitial iron is one of the impurities that is internally gettered in this way. In fact it is striking to notice the strong anti-correlation between the two images in Figure 7 – regions of low lifetime correspond to

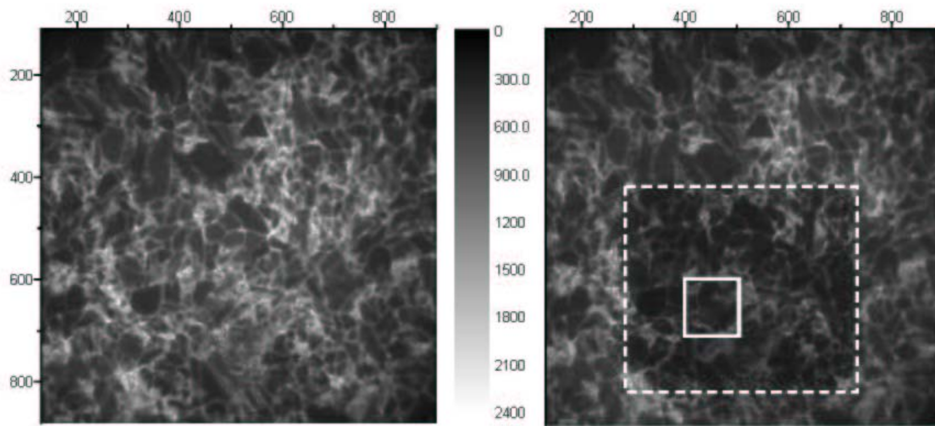

Figure 6: *PL images of an as-cut mc-Si wafer (#69a) before (left) and after (right) FeB pair dissociation. The scale indicates the number of counts in the 1 second exposure time. The dotted square shows the region illuminated to break the FeB pairs, and the solid square the region analysed to generate an iron image. The scale shows the PL count rate.*

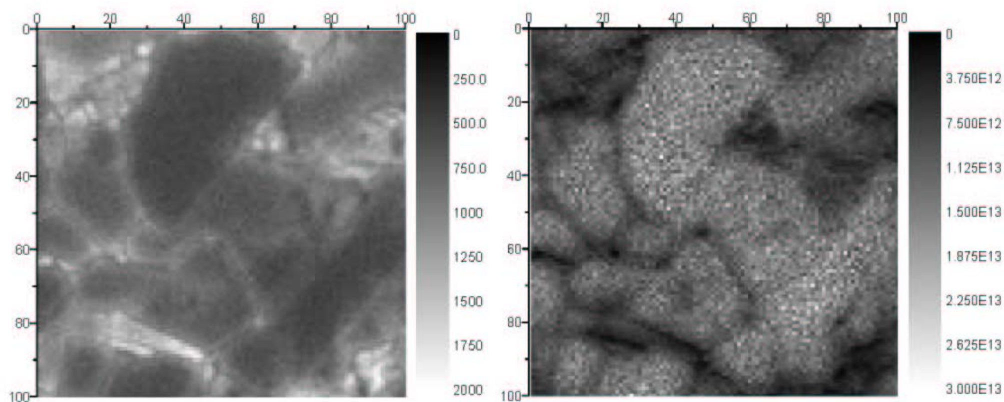

Figure 7: *Enlarged PL image before pair dissociation (left) of the small region shown in Figure 6 of wafer #69a, and the corresponding iron image (right). The left scale shows the PL count rate, the right scale the iron concentration in units cm^{-3}.*

regions of high [Fe_i]. This would suggest that Fe_i has a strong impact on the carrier lifetime in wafers from this region of a mc-Si ingot. Indeed we know this to be true from other measurements of [Fe_i] based on QSSPC lifetime measurements [47].

The average value of [Fe_i] in the iron image of Figure 7 is 9×10^{12} cm^{-3}. This compares well with the average [Fe_i] measured on this wafer using the QSSPC technique [47], which was 7×10^{12} cm^{-3}. In fact we found very good agreement between the two methods for six mc-Si wafers from different sections of an ingot, with [Fe_i] values ranging from 1×10^{11} up to 7×10^{12} cm^{-3}.

Figure 8 shows a similar pair of images for a wafer from close to the top of the ingot. In this case the carrier lifetime is higher, as indicated by the greater count rate in the PL image on the left. Again the grain boundaries are prominent, but there is no 'denuded zone' around the grain boundaries with a higher lifetime. Instead, the highest lifetime regions are deep within the grains. The corresponding iron image shows that [Fe_i] is lower than in Figure 7. In fact the average value was 6.5×10^{11}, very close to the QSSPC-derived average [Fe_i] value of 6×10^{11} cm^{-3}. Again, the [Fe_i] is reduced near the grain boundaries, indicating precipitation of Fe there. Note however that there are several sub-grain boundaries evident in the PL figure on the left, but these do not seem to cause a local reduction in [Fe_i]. This suggests that these extended defects do not act as strong precipitation sites, unlike the random-angle grain boundaries. Similar observations have been made previously, on the basis of EBIC [48,49] and synchrotron microprobe-XRF measurements [50,51].

We believe that such an iron imaging technique will prove useful for studying the behaviour of iron, and by analogy several other metal impurities, in photovoltaic silicon materials such as multicrystalline and ribbon silicon. This is especially relevant considering the advent of less pure solar-grade silicon feedstock materials.

An important reason for the apparent success of PL imaging applied to the generation of iron images is the speed with which the PL images can be generated (1 second under 1 sun was used here). This enables the initial measurement to be carried out with minimal breaking of FeB pairs.

7 CONCLUSIONS

We have reviewed some of the most important impurities found in directionally-solidified ingot-grown multicrystalline silicon, and some techniques used to

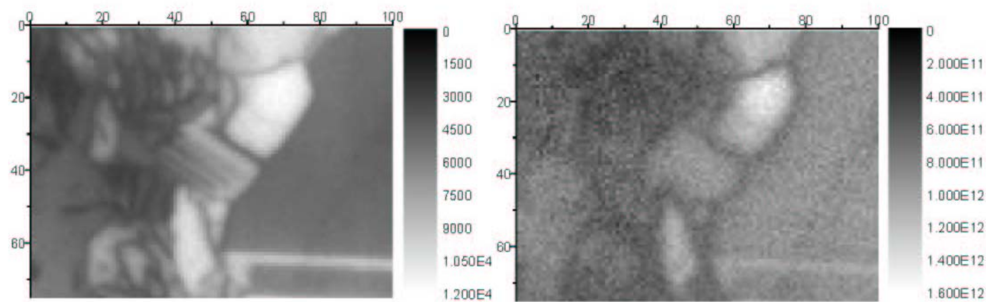

Figure 8: *Enlarged PL image before pair dissociation (left) of wafer #355a, and the corresponding iron image (right). The left scale shows the PL count rate, the right scale the iron concentration in units cm^{-3}.*

detect them. We have also introduced a new method for rapid imaging of the interstitial iron concentrations in silicon wafers based on band-to-band photoluminescence imaging.

Acknowledgements: D.M. is supported by an Australian Research Council Fellowship. The Centre of Excellence for Advanced Silicon Photovoltaics and Photonics is supported by the Australian Research Council. The authors thank Rob Elliman from the Research School of Physical Science and Engineering, ANU, for access to the ion implanter, and Eugenia Sepulveda for assisting with the FZ sample preparation.

[1] J. Schmidt and K. Bothe, Phys. Rev. B 69 (2004) 024107.
[2] T. Buonassisi*, et al.*, Progress in Photovoltaics: Research and Applications 14 (2006) 513.
[3] M. J. Keevers, A. Turner, U. Schubert, P. A. Basore and M. A. Green, Proc. 20th Europ. PVSEC, Barcelona, Spain (2005)
[4] A. A. Istratov*, et al.*, J. Appl. Phys. 94 (2003) 6552.
[5] A. A. Istratov, W. Huber and E. R. Weber, Appl. Phys. Lett. 85 (2004) 4472.
[6] D. Macdonald, A. Cuevas, A. Kinomura, Y. Nakano and L. J. Geerligs, J. Appl. Phys. 97 (2005) 033523.
[7] S. A. McHugo, A. Thompson, I. Perichaud and S. Martinuzzi, Appl. Phys. Lett. 72 (1998) 3482.
[8] S. A. McHugo*, et al.*, J. Appl. Phys. 89 (2001) 4282.
[9] A. Bentzen, A. Holt, R. Kopecek, G. Stokkan, J. S. Christensen and B. G. Svensson, J. Appl. Phys. 99 (2006) 093509.
[10] T. Buonassisi*, et al.*, J. Appl. Phys. 97 (2005) 074901.
[11] K. Graff, *"Metal Impurities in Silicon-Device Fabrication"*, Springer-Verlag, Berlin, 2000.
[12] G. Zoth and W. Bergholz, J. Appl. Phys. 67 (1990) 6764.
[13] D. Macdonald and L. J. Geerligs, Appl. Phys. Lett. 85 (2004) 4061.
[14] I. Périchaud and S. Martinuzzi, Proceedings 22nd IEEE Photovoltaic Specialists Conference, Las Vegas, USA (1991) 877.
[15] L. L. Kazmerski, P. J. Ireland and T. F. Ciszek, Appl. Phys. Lett. 36 (1980) 323.
[16] Y. Tian, Y.-L. Jiang, Y. Chen, F. Lu and B.-Z. Li, Semicond. Sci. Technol. 17 (2002) 83.
[17] M. Kittler, W. Seifert and K. Knobloch, Microeletronic Engineering 66 (2003) 281.
[18] D. Karg, G. Pensl, M. Schulz, C. Hässler and W. Koch, Phys. Stat. Sol. (b) 222 (2000) 379.
[19] O. Klettke, D. Karg, G. Pensl, M. Schulz, G. Hahn and T. Lauinger, Proceedings 12th International Photovoltaic Science and Engineering Conference, Jeju, Korea (2001) 617.
[20] S. H. Park and D. K. Schroder, J. Appl. Phys. 78 (1995) 801.
[21] L. Jastrzebski, L. Lagowski, W. Henley, D. Schielein, S. G. Balster and D. K. Schroder, Proceedings 12th European Photovoltaic Solar Energy Conference, Amsterdam, The Netherlands (1994) 52.
[22] J. Lu, M. Wagener, G. Rozgonyi, J. Rand and R. Jonczyk, J. Appl. Phys. 94 (2003) 140.
[23] K. Mishra, Appl. Phys. Lett. 68 (1996) 3281.
[24] K. Bothe, R. Sinton and J. Schmidt, Progress in Photovoltaics: Research and Applications 13 (2005) 287.
[25] J. Schmidt, Appl. Phys. Lett. 82 (2003) 2178.
[26] W. Seifert, M. Kittler and J. Vanhellemont, Materials Science and Engineering B 42 (1996) 260.
[27] E. Simoen*, et al.*, Materials Science and Engineering B 102 (2003) 207.
[28] L. J. Geerligs, Proceedings 12th Workshop on Crystalline Silicon Solar Cell Materials and Processes, Breckenridge, CO (2002) 280.
[29] M. Porrini, I. Crössman, M. G. Pretto, R. Scala and R. Wolf, Solid State Phenom. 108-109 (2005) 591.
[30] N. Inoue and M. Nakatsu, Solid State Phenom. 108-109 (2005) 621.
[31] N. Inoue*, et al.*, Solid State Phenom. 108-109 (2005) 609.
[32] L. J. Geerligs, D. Macdonald and G. Coletti, 17th NREL Workshop on Crystalline Silicon Solar Cells & Modules: Materials and Processes, Vail, Colorado (2007)
[33] J. Lagowski, P. Edelman, M. Dexter and W. Henley, Semicond. Sci. Technol. 7 (1992) A185.
[34] L. Jastrzebski, W. Henley, D. Schielein and J. Lagowski, J. Electrochem. Soc. 142 (1995) 3869.
[35] D. K. Schroder, Meas. Sci. Technol. 12 (2001) R16.
[36] O. Palais, S. Martinuzzi and J. J. Simon, Mat. Sci. Semi. Process. 4 (2001) 27.
[37] M. Bail, J. Kentsch, R. Brendel and M. Schulz, Proc. 28th IEEE PVSC, Anchorage, Alaska (2000) 99.
[38] J. Isenberg, S. Riepe, S. W. Glunz and W. Warta, J. Appl. Phys. 93 (2003) 4268.
[39] T. Trupke, R. A. Bardos, M. C. Schubert and W. Warta, Appl. Phys. Lett. 89 (2006) 044107.

[40] J. Henze*, et al.*, Proc. 20th Europ. PVSEC, Barcelona (2005) 769.
[41] D. Macdonald, L. J. Geerligs and A. Azzizi, J. Appl. Phys. 95 (2004) 1021.
[42] R. A. Bardos, T. Trupke, M. C. Schubert and T. Roth, Appl. Phys. Lett. 88 (2006) 053504.
[43] A. A. Istratov, H. Hieslmair and E. R. Weber, Appl. Phys. A 69 (1999) 13.
[44] M. J. Kerr and A. Cuevas, J. Appl. Phys. 91 (2002) 2473.
[45] D. Macdonald, T. Roth, P. N. K. Deenapanray, T. Trupke and R. A. Bardos, Appl. Phys. Lett. 89 (2006) 142107.
[46] L. J. Geerligs and D. Macdonald, Appl. Phys. Lett. 85 (2004) 5227.
[47] J. Tan, D. Macdonald, N. Bennet, D. Kong, A. Cuevas and I. Romijn, Appl. Phys. Lett. 91 (2007) 043505.
[48] M. Kittler, W. Seifert, M. Stemmer and J. Palm, J. Appl. Phys. 77 (1995) 3725.
[49] J. Chen, T. Sekiguchi, D. Yang, F. Yin, K. Kido and S. Tsurekawa, J. Appl. Phys. 96 (2004) 5490.
[50] T. Buonassisi, A. A. Istratov, M. D. Pickett, M. A. Marcus, T. F. Ciszek and E. R. Weber, Appl. Phys. Lett. 89 (2006) 042102.
[51] K. Arafune, E. Ohishi, H. Sai, Y. Terada, Y. Ohshita and M. Yamaguchi, Jpn. J. Appl. Phys. 45 (2006) 6153.